# Evolution of Quantum Fluctuations Near the Quantum Critical Point of the Transverse Field Ising Chain System CoNb 2 O 6

# Quantum Fluctuations of the Transverse Field Ising Chain

A. W. Kinross[1], M. Fu[1], T. J. Munsie[1], H. A. Dabkowska[2], G. M. Luke[1,3], S. Sachdev[4], and T. Imai[1,3*]
[1]*Department of Physics and Astronomy, McMaster University, Hamilton L8S4M1, Canada*
[2]*Brockhouse Institute for Materials Research, McMaster University, Hamilton L8S4M1, Canada*
[3]*Canadian Institute for Advanced Research, Toronto, Ontario M5G1Z8, Canada and*
[4]*Department of Physics, Harvard University, Cambridge, Massachusetts 02138, USA*
(Dated: January 28, 2014)



**The concept of $T = 0$ quantum phase transitions has emerged as an overarching theme in strongly correlated electron physics [1–9]. The nature of quantum fluctuations near the quantum critical point, however, remains enigmatic [10]. How well does the quantum criticality account for finite temperature properties? How high in temperature does the effect of the quantum critical point persist?[10, 11] The dearth of appropriate model materials has not permitted experimentalists to address these fundamental questions even for the transverse field Ising chain (TFIC), a celebrated textbook example of quantum criticality [6]. Here we use NMR (Nuclear Magnetic Resonance) to map the evolution of quantum spin fluctuations in $CoNb_2O_6$ [12–14], which has recently been proposed as an ideal model material for the TFIC [15, 16]. We will demonstrate that the effect of the quantum critical point persists to a remarkably high temperature, $T \sim 0.4J$, where the exchange coupling $J$ is the only energy scale in the problem.**

The TFIC Hamiltonian is deceptively simple [6];

$$H = -J \sum_i (\sigma_i^z \sigma_{i+1}^z + g\sigma_i^x), \qquad (1)$$

where $J$ ($> 0$ for ferromagnetic Ising chains in $CoNb_2O_6$) represents the nearest-neighbor spin-spin exchange interaction, $\sigma_i^{z(x)}$ is the z(x)-component of the Pauli matrix at the i-th site, and the dimensionless coupling constant $g$ is related to the transverse magnetic field $h_\perp$ applied along the x-axis as $g = h_\perp/h_\perp^c$, where $h_\perp^c$ is the critical field ($h_\perp^c = 5.25 \pm 0.15$ Tesla in $CoNb_2O_6$, as shown below). Since $\sigma_i^z$ and $\sigma_i^x$ do not commute, the classical Ising Hamiltonian for $g = 0$ becomes the quantum TFIC Hamiltonian for $g > 0$. The QCP (Quantum Critical Point) is located at $g = 1$, where the applied field is tuned precisely at $h_\perp^c$; a magnetic field greater than $h_\perp^c$ coerces the magnetic moments along its direction and destroys the $T = 0$ ferromagnetic ground state. See Fig. 1(a) for the generic theoretical phase diagram of the TFIC [6, 17]. In spite of its apparent simplicity, the TFIC served as the foundational model for the quantum Monte Carlo simulations [18], and continues to attract attention in quantum information theory [19].

A major advantage of working with the TFIC as a model system for testing the fundamental ideas of QPT's (Quantum Phase Transitions) is that, in the absence of a transverse magnetic field ($g = 0$), the thermodynamic properties of the Ising chain can be rigorously solved at arbitrary temperatures [20]. Even in a finite transverse field ($g > 0$), the TFIC is well understood at $T = 0$ [18, 21], and QC (Quantum Critical) scaling theory extended the $T = 0$ results to finite temperatures [6, 17].

Our primary goals here are to (a) experimentally test the phase diagram of the TFIC in Fig. 1(a) above $T = 0$, and (b) demonstrate that the effect of the QCP persists to $T \sim 0.4J$, based on NMR measurements of $CoNb_2O_6$. NMR is a powerful low energy probe, and good at probing the physical properties near QCP's [22–28]. In what follows, we take advantage of the hyperfine interactions between Co electrons and $^{93}$Nb nuclear spins. Based on the measurement of the nuclear spin-lattice relaxation rate $1/T_1$ at the non-magnetic $^{93}$Nb sites, we map the evolution of low energy quantum fluctuations of Co spins near the QCP. See Supplementary Information for the details of NMR data acquisition.

We show the crystal structure of $CoNb_2O_6$ in Fig. 2 [29]. The Co-O-Co chains propagate along the c-axis, and the easy axis of the Co moments lies within the ac-plane [12, 13]. The ferromagnetic super-exchange interaction between the nearest-neighbor Co ions is estimated to be $J = 17 \sim 23$ K, based on ESR [14] and neutron scattering [15] measurements. The inter-chain couplings between adjacent Co chains are antiferromagnetic [12, 15], weaker than $J$ by an order of magnitude [14, 15], and frustrated [12, 16]. This means that the three-dimensional (3D) magnetic long range order induced by inter-chain interactions, which tends to mask the effects of the 1D QCP of the individual Ising chains, is suppressed; the 3D ordering temperature is as low as $T_c^{3D} = 2.9$ K even in $h_\perp = 0$ [12, 13]. Combined with the modest $J$, $CoNb_2O_6$ is an ideal model material for the TFIC, but was overlooked for three decades. Very recently, Coldea et al. demonstrated that the application of $h_\perp$ along the b-axis induces a QPT from the 3D ordered state to a paramagnetic state above the 3D critical field, $h_\perp^{c,3D} = 5.5$ Tesla [15, 30].

In Fig. 3, we summarize the $T$ and $h_\perp$ dependences of $1/T_1$. Notice that $1/T_1$ varies by more than three orders of magnitude between $h_\perp = 3$ and 9 Tesla. Quite generally, $1/T_1$ probes the wave vector **k**-integral within the first Brillouin zone of the dynamical spin structure factor

*Electronic address: imai@mcmaster.ca

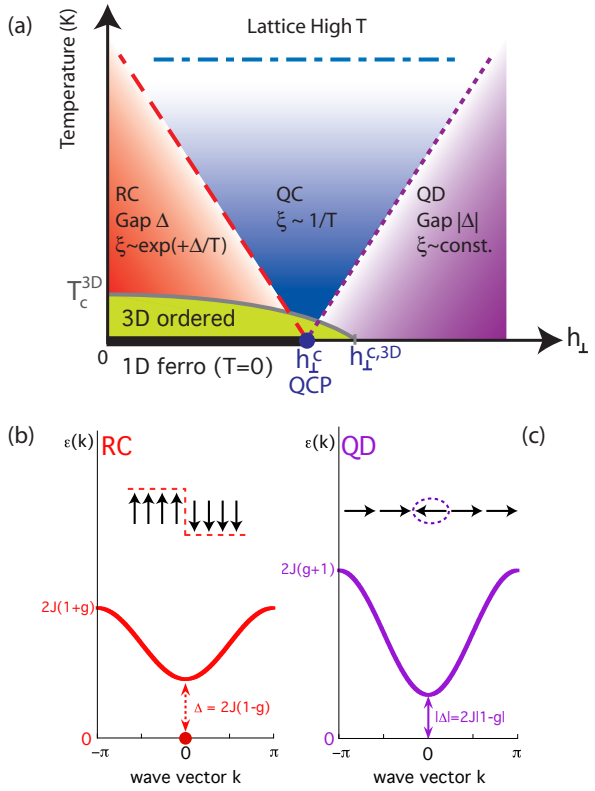


FIG. 1: Phase diagram and excitation spectra of the TFIC. (a) A generic $T - h_\perp$ phase diagram of the TFIC encompasses three scaling regimes with distinct behaviors of the spin-spin correlation length $\xi$: RC (Renormalized Classical, $g < 1$ hence $h_\perp < h_\perp^c$, and $\xi \sim \exp(+\Delta/T)$), QC (Quantum Critical, $\xi \sim 1/T$), and QD (Quantum Disordered, $g > 1$ hence $h_\perp > h_\perp^c$, and $\xi \sim$ constant) [6]. The dashed and dotted lines represent the crossover temperature from the QC to RC regime at $T \sim \Delta$ and from the QC to QD regime at $T \sim |\Delta|$, respectively. An isolated 1D Ising chain would exhibit ferromagnetic long range order only at $T = 0$ below $h_\perp^c$, but the 3D inter-chain couplings lead to a 3D order at $T > 0$ up to $h_\perp^{c,3D}$ ($> h_\perp^c$). (b) The spin excitation spectrum in the RC regime has two components, the quasi-elastic peak at the origin (represented by a filled dot) and the propagating domain walls (inset). The dispersion of the latter is $\epsilon(k) = J[2 - 2g\cos(k) + O(g^2)]$, with an excitation gap $\Delta = 2J(1-g)$ [6]. The quasi-elastic peak becomes a Bragg peak when $\xi$ diverges toward the 1D ferromagnetic long range order at $T = 0$. (c) The spin excitation spectrum in the QD regime, $\epsilon(k) = Jg[2 - (2/g)\cos(k) + O(1/g^2)]$ with a gap $|\Delta| = 2|1-g|$ [6], arises from the propagation of flipped spins (inset). Unlike the RC regime, there is no quasi-elastic peak.

$S(\mathbf{k}, \omega_n)$ at the NMR frequency $\omega_n/2\pi$ ($\sim 50$ MHz):

$$1/T_1 = \sum_{\mathbf{k}} |a_{hf}|^2 S(\mathbf{k}, \omega_n), \qquad (2)$$

where $a_{hf}$ is the hyperfine coupling between the observed nuclear spin and Pauli matrices. In essence, $1/T_1$ measures the strength of Co spin fluctuations at the time scale set by the NMR frequency. Our $1/T_1$ data at low

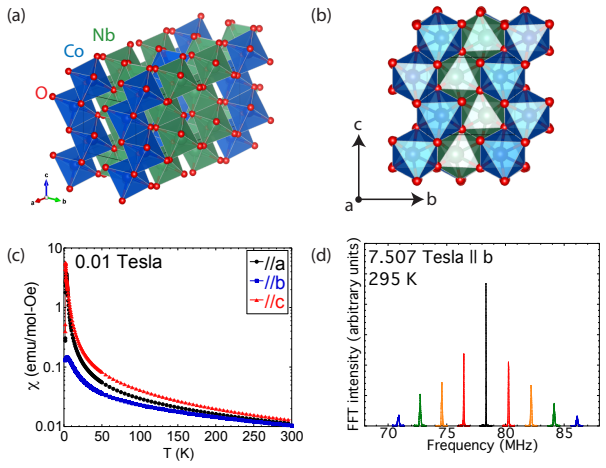


FIG. 2: Structure and basic properties of $CoNb_2O_6$. (a) The crystal structure of $CoNb_2O_6$. (b) Both magnetic $CoO_6$ and non-magnetic $NbO_6$ octahedra form a chain along the c-axis, as seen from the a-axis direction. The transverse field $h_\perp$ is applied along the b-axis. (c) Magnetic susceptibility $\chi$ of the $CoNb_2O_6$ single crystal measured in 0.01 Tesla. (d) The $^{93}$Nb NMR lineshape at 295 K obtained by the FFT of spin echo signals. Since the $^{93}$Nb nuclear spin is $I = 9/2$, we observe 4 pairs of satellite transitions split by a quadrupole frequency $\nu_Q^b = 1.9$ MHz, in addition to the central peak arising from the $I_z = +\frac{1}{2}$ to $-\frac{1}{2}$ transition.

temperatures exhibits two distinct field regimes. Below $h_\perp \sim 5.3$ Tesla, $1/T_1$ diverges gradually toward $T = 0$, signaling the critical slowing down of Co spin fluctuations in the RC (Renormalized Classical [2]) regime of Fig. 1(a) toward the $T = 0$ ferromagnetic ground state of each individual Ising chain. In other words, the spectral weight of the Co spin-spin correlation function grows at the quasi-elastic peak located at $k = 0$ in Fig. 1(b) below $h_\perp \sim 5.3$ Tesla. The Co spin-spin correlation length $\xi$ along the chain grows as $\xi \sim \exp(+\Delta/T)$ in the RC regime [6], where $\Delta$ is the gap in the spin excitation spectrum as defined in Fig. 1(b). Accordingly, we expect $1/T_1 \sim \exp(+\Delta/T)$ for $T \ll \Delta$. See Supplementary Information for the details of the theory and data analysis of $1/T_1$. In contrast, $1/T_1$ observed above $h_\perp \sim 5.3$ Tesla saturates and begins to decrease with temperature, signaling the opening of a spin excitation gap in the Quantum Disordered (QD) regime in Fig. 1(a). The behavior of $1/T_1$ is therefore dominated by the thermal activation of spin excitations across the gap, $|\Delta|$, as defined in Fig. 1(c). Therefore we expect $1/T_1 \sim \exp(-|\Delta|/T)$ for $T \ll |\Delta|$. We have thus identified the 1D QCP of each individual Ising chain as $h_\perp^c \sim 5.3$ Tesla.

In Fig. 4(a), we present the exponential fit of $1/T_1 \sim \exp(\Delta/T)$ with $\Delta$ as a free parameter. The fitting range barely satisfies $T < |\Delta|$ near $h_\perp \sim 5.3$ Tesla, and hence we conducted a scaling analysis of $1/T_1$ to improve the accuracy of $\Delta$. We summarize the $h_\perp$ dependence of $\Delta$ in Fig. 4(b). Remarkably, we found that $\Delta$ varies linearly

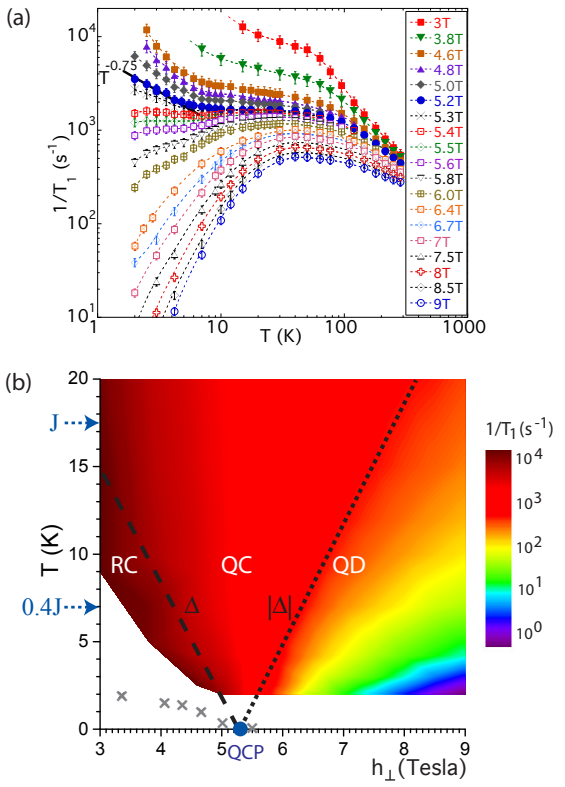


FIG. 3: $^{93}$Nb NMR relaxation rate $1/T_1$. (a) The temperature dependence of $1/T_1$ in $h_\perp$ applied along the b-axis. All dashed lines interconnecting the data points are guides for the eye. The black solid line represents a power-law fit, $1/T_1 \sim 6.2 \times 10^3\ T^{-0.75}\ \mathrm{s}^{-1}$. (b) A colour plot of $1/T_1$. The dashed (dotted) line represents the expected crossover temperature $\Delta$ ($|\Delta|$) from the QC to RC (QD) regime, based on the linear $h_\perp$ dependence of $\Delta$ estimated in Fig. 4(b). Also shown (grey x) is the 3D ordering temperature $T_c^{3D}$ [30].

with $h_\perp$. This linear behavior is precisely what we expect from the theoretical prediction for the nearest-neighbor quantum Ising chain, $\Delta = 2J(1 - h_\perp/h_\perp^c)$ [6]. From the intercepts of the linear fit with the horizontal and vertical axes, we estimate $h_\perp^c = 5.25 \pm 0.15$ Tesla and $J = 17.5^{+2.5}_{-1.5}$ K, respectively, in excellent agreement with earlier reports [14, 15].

We present the colour plot of $1/T_1$ in Fig. 3(b). Also shown in Fig. 3(b) is the crossover temperatures, $\Delta$ and $|\Delta|$, based on the linear fit in Fig. 4(b). Our colour plot visually captures the crossover from the QC regime to the RC and QD regimes successfully. We are the first to verify the theoretical $T - h_\perp$ phase diagram in Fig. 1(a) for finite temperatures, $T > 0$, using an actual model material.

Having established the phase diagram of the TFIC in $CoNb_2O_6$, we are ready to test its quantum criticality in the QC regime located between the RC and QD regimes. At the 1D critical field $h_\perp^c$, we applied QC scaling to

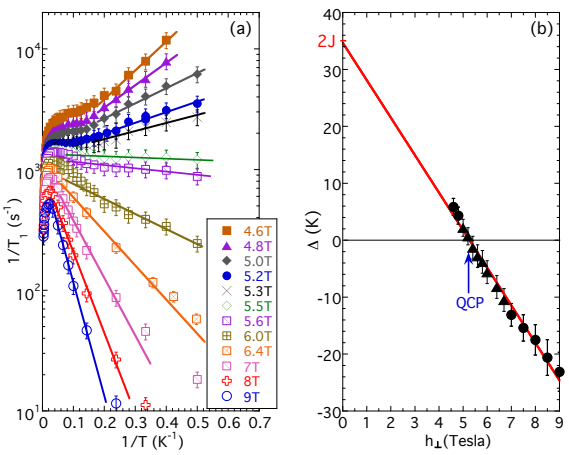


FIG. 4: Estimation of the gap $\Delta$. (a) The exponential fit $1/T_1 \sim \exp(\Delta/T)$ for representative values of $h_\perp$. (b) • represents $\Delta$ as determined from (a), while ▲ is based on the scaling analysis (see Supplementary Information). Also shown is a linear fit, $\Delta = 2J(1 - h_\perp/h_\perp^c)$. From the fit, we estimate $h_\perp^c = 5.25 \pm 0.15$ Tesla and $J = 17.5^{+2.5}_{-1.5}$ K.

eq.(2), and obtained

$$1/T_1 = 2.13\ |a_{hf}|^2 J^{-0.25} T^{-0.75}. \qquad (3)$$

We fitted the $1/T_1$ data observed at 5.2 Tesla to eq.(3) with $J = 17.5$ K, and found $|a_{hf}/\hbar|^2 = 7.6 \times 10^{14}\ \mathrm{s}^{-2}$. It is important to realize that our experimental data exhibits the expected power-law behavior, $1/T_1 \sim T^{-0.75}$, up to $\sim 7$ K, which corresponds to $\sim 0.4J$. Our finding therefore addresses an important and unresolved question that has been facing the strongly correlated electrons community for years: *How high in temperature does the effect of the QCP persist?* For the TFIC, the quantum fluctuations originating from the zero temperature QCP persist up to as high as $T \sim 0.4J$. Our experimental finding is consistent with the earlier theoretical analysis of the QC scaling function for the TFIC [11].

We mark the upper bound of the QC scaling regime, $T \sim 0.4J$, in Fig. 3(b) with a horizontal arrow. Such a robust quantum criticality observed at finite temperatures above the QCP is in stark contrast with the case of thermally induced *classical* phase transitions; the critical region of the latter generally narrows as the phase transition temperature approaches zero, and eventually diminishes at $T = 0$ [10]. Many authors have constructed analogous colour plots for different parameters (such as electrical resistivity, as an example) for a variety of strongly correlated electron systems, including copper-oxide and iron-pnictide high $T_c$ superconductors and heavy Fermion systems [8, 9]. The aim of these authors was to build a circumstantial case that quantum fluctuations persist at finite temperatures far above the QCP. Fig. 3b is a rare example for the solvable TFIC Hamiltonian, and the overall similarity to the case of high $T_c$ cuprates and other exotic superconductors gives

us hope that quantum fluctuations may indeed account for the mechanism of exotic superconductivity.


[1] Hertz, J. A. Quantum critical phenomena. Phys. Rev. B **14**, 1165-1184 (1976).

[2] Chakravarty, S. Halperin, B. I. and Nelson, D. R. Two-dimensional quantum Heisenberg antiferromagnet at low temperatures. Phys. Rev. B **39**, 2344-2371 (1989).

[3] Millis, A. J. Effect of a nonzero temperature on quantum critical points in itinerant fermion systems. Phys. Rev. B **48**, 7183-7196 (1993).

[4] Chubukov, A. Sachdev, S. and Ye, J. Theory of two-dimensional quantum Heisenberg antiferromagnets with a nearly critical ground state. Phys. Rev. B **49**, 11919-11961 (1994).

[5] Goldman, A. M. and Markovic, N. Superconductor-insulator transitions in the two-dimensional limit. Physics Today **51(11)**, 39-44 (1998).

[6] Sachdev, S. *Quantum phase transitions (1st Ed.)*. (Cambridge University Press, Cambridge, 1999).

[7] Sachdev S. Quantum magnetism and criticality. Nature Physics **4**, 173-185 (2008).

[8] Gegenwart, P. Si, Q. and Steglich, F. Quantum criticality in heavy-Fermion metals. Nature Physics **4**, 186-197 (2008).

[9] Sachdev, S. and Keimer, B. Quantum criticality. Physics Today **64(2)**, 29-35 (2011).

[10] Lonzarich, G. R. Magnetic quantum liquid enigma. Nature Physics **1**, 11-12 (2005).

[11] Kopp, A. and Chakravarty, S. Criticality in correlated quantum matter. Nature Physics **1**, 53-56 (2005).

[12] Scharf, W. Weitzel, H. Yaeger, I. Maartense, I. and Wanklyn, B. M. Magnetic structures of $CoNb_2O_6$. J. Magn. Magn. Mater. **13**, 121-124 (1979).

[13] Hanawa, T. et al., Anisotropic specific heat of $CoNb_2O_6$ in magnetic fields. J. Phys. Soc. Jpn. **63**, 2706-2715 (1994).

[14] Kunimoto, T. et al., Submillimeter wave ESR study of magnetic excitations in the Ising ferromagnetic chain $CoNb_2O_6$. J. Phys. Soc. Jpn. **68**, 1703-1710 (1999).

[15] Coldea, R. et al., Quantum Criticality in an Ising Chain: Experimental Evidence for Emergent $E_8$ Symmetry. Science **327**, 177-180 (2010).

[16] Lee, S. Kaul, R. K. and Balents, L. Interplay of quantum criticality and geometric frustration in columbite. Nature Physics **6**, 702-706 (2010).

[17] Sachdev, S. and Young, A. P. Low temperature relaxational dynamics of the Ising chain in a transverse field. Phys. Rev. Lett. **78**, 2220-2223 (1997).

[18] Suzuki, M. Relationship between d-dimensional quantum spin systems and (d+1)-dimensional Ising systems. Prog. Theor. Phys. **56**, 1454-1469 (1976).

[19] Zhang, J. et al., Direct observation of quantum criticality in Ising spin chains. Phys. Rev. A **79**, 012305 (2009).

[20] Binney, J. J. Dowrick, N. J. Fisher, A. J. and Newman, M. E. J. *The theory of critical phenomena* (Oxford University Press, Oxford, 1992).

[21] Chakrabarti, B. K. Dutta, A. and Sen, P. *Quantum Ising phases and transitions in transverse Ising models*. (Springer-Verlag, Berlin, 1996).

[22] Imai, T. Slichter, C. P. Yoshimura, K. and Kosuge, K. Low frequency spin dynamics in undoped and Sr-doped $La_2CuO_4$. Phys. Rev. Lett. **70**, 1002-1005 (1993).

[23] Mukhopadhyay, S. et al., Quantum-critical spin dynamics in quasi-one-dimensional antiferromagnets. Phys. Rev. Lett. **109**, 177206 (2012).

[24] Vyaselev, O. Takigawa, M. Vasiliev, A. Oosawa, A. and Tanaka, H. Field-induced magnetic order and simultaneous lattice deformation in $TlCuCl_3$. Phys. Rev. Lett. **92**, 207202 (2004).

[25] Kuehne, H. et al., Dynamics of a Heisenberg spin chain in the quantum critical regime: NMR experiment versus effective field theory. Phys. Rev. B.**83**, 100407(R) (2011).

[26] Ning, F. L. et al. Contrasting spin dynamics between underdoped and overdoped $Ba_2(Fe_{1-x}Co_x)_2As_2$. Phys. Rev. Lett. **104**, 037001 (2010).

[27] Nakai, Y. et al. Unconventional superconductivity and antiferromagnetic quantum critical behavior in the isovalent-doped $Ba_2Fe_2(As_{1-x}P_x)_2$. Phys. Rev. Lett. **105**, 100703 (2010).

[28] Zhou, R. et al., Quantum criticality in electron-doped $Ba_2Fe_{2-x}Ni_xAs_2$. Nature Communications **4**, 2265 (2013).

[29] Husson, E. Repelin, Y. Dao, N. Q. and Brusset, H. Characterization of different bondings in some divalent metal niobates of columbite structure. Mat. Res. Bull. **12**, 1199-1206 (1977).

[30] da Silva Wheeler, E. M., *Neutron Scattering from Low-Dimensional Quantum Magnets* (Ph.D. Thesis, Oxford University, 2007).



**Acknowledgements**

T.I. and S.S. thank helpful communications with A. P. Young, Y. Itoh, B. Gaulin, M. P. Gelfand and T. Sakai. The work at McMaster was supported by NSERC and CIFAR. S.S. acknowledges the financial support from NSF.


**Author contributions**

A.W.K., M.F., and T.I. conducted NMR measurements. T.J.M., A.W.K., and G.M.L. grew the single crystal, and characterized its bulk properties. H.A.D. participated in the crystal growth. S.S. derived the theoretical formulae for $1/T_1$. T.I. conceived the project, and wrote the manuscript with input from all authors.

**Competing financial interests**

The authors declare no competing financial interests.

## Supplementary Information

### 1. NMR Measurements of $1/T_1$

We grew the $CoNb_2O_6$ single crystal from a stoichiometric mixture of cobalt and niobium oxides using a floating zone furnace. We assessed the surface quality and oriented the crystal utilizing Laue x-ray diffractometry. Once the material was sectioned into oriented slices along the a, b and c crystallographic directions, these were individually scanned with the Laue diffractometer and showed a uniform, single-crystalline structure. A small section of the single crystal was ground into a powder and analyzed using powder x-ray diffraction which showed only single phase cobalt niobate in the crystal within instrument resolution. The features present in the SQUID magnetometry data matched previously published data on this material. All the pictorial images of the crystal structure in this paper were drawn using VESTA [S1].

For NMR measurements, we cut a piece of single crystal with the approximate dimensions of 4 mm x 2 mm x 5 mm. We glued the crystal to a sturdy sample holder made of machinable aluminum-oxide (MACOR ceramic) with a thickness of $\sim 3$ mm to ensure that the crystal orientation did not change at low temperatures. We found that the strong magnetic torque applied to the crystal by the external magnetic field could easily bend sample holders made of soft materials such as plexiglass or plastic, and introduce noticeable systematic errors below $\sim 10$ K.

We measured the $^{93}$Nb ($I = 9/2$) nuclear spin-lattice relaxation rate $1/T_1$ primarily at the central transition between the $I_z = +\frac{1}{2}$ and $I_z = -\frac{1}{2}$ energy levels. The central transition is the strongest among all 9 peaks in Fig. 2(d), and hence most advantageous in terms of the signal intensity. We summarize the temperature dependence of the NMR lineshape for the central transition in Fig. S1. We applied an inversion $\pi$ pulse prior to the $\pi/2 - \pi$ spin echo sequence, and monitored the recovery of the spin echo intensity $M(t)$ as a function of the delay time $t$. The typical width of the $\pi/2$ pulse is $\sim 1\mu$s. An example of the signal recovery of the central transition observed at 130 K in $h_\perp = 3$ Tesla is shown in Fig. S2, in comparison to that observed for a fourth satellite transition between the $I_z = \pm\frac{9}{2}$ and $I_z = \pm\frac{7}{2}$ energy levels on the higher frequency side.

We fitted these recovery curves to the solutions to the rate equation [S2]:

$$M(t) = M(\infty) - A\sum_{j=1}^{9} a_j e^{-b_j t/T_1}, \qquad (1)$$

with three free parameters: $M(\infty)$, $A$, and $1/T_1$. By solving the coupled rate equations for $I = \frac{9}{2}$ under the appropriate initial condition, one can calculate and fix the coefficients as $(a_1, a_2, a_3, a_4, a_5, a_6, a_7, a_8, a_9) = (0.653, 0, 0.215, 0, 0.092, 0, 0.034, 0, 0.06)$ for the central transition and (0.001, 0.0112, 0.0538, 0.1485, 0.2564, 0.2797, 0.1828, 0.0606, 0.0061) for the fourth satellite transitions, while $(b_1, b_2, b_3, b_4, b_5, b_6, b_7, b_8, b_9) = (45, 36, 28, 21, 15, 10, 6, 3, 1)$ for both cases [S2]. Our results in Fig. S2 confirm that the best fit values of $1/T_1$ agree within $\sim$ 2 % between the central and satellite transitions.

When the relaxation rate exceeds $1/T_1 \sim 2 \times 10^3$ s$^{-1}$, accurate measurements of $1/T_1$ using the central transition become increasingly difficult because the recovery curve $M(t)$ is dominated by two extremely

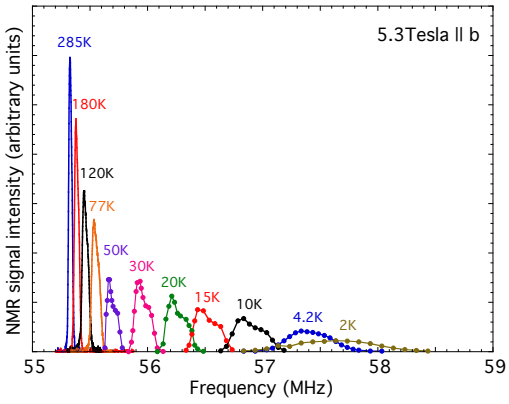


FIG. S1: The temperature dependence of the $^{93}$Nb NMR lineshape observed for the central transition between the $I_z = +\frac{1}{2}$ and $I_z = -\frac{1}{2}$ energy levels in $h_\perp = 5.3$ Tesla. We obtained the lineshapes using the FFT of the spin echo signal above 77 K. For the broader lineshapes below 77 K, we measured the integral of the spin echo as a function of the frequency.

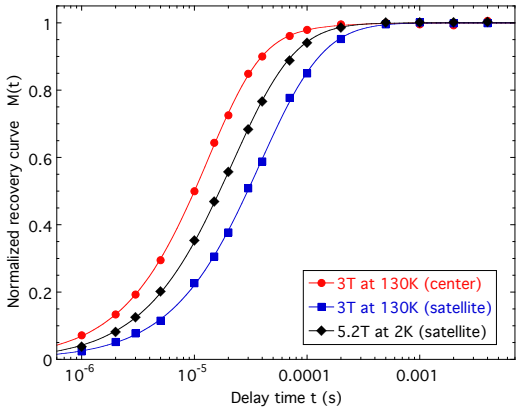


FIG. S2: Examples of the recovery of the spin echo intensity, $M(t)$, observed for the central and a fourth satellite transition at 130 K in $h_\perp = 3$ Tesla. For comparison, we normalized the recovery curves by plotting $1 - [M(\infty) - M(t)]/A$ as a function of $t$. The solid lines represent the best fit with $1/T_1 = 1.99 \times 10^3$ s$^{-1}$ for the central transition and $1/T_1 = 1.96 \times 10^3$ s$^{-1}$ for the fourth satellite transition, as described in the text. Also plotted is the recovery curve observed for the fourth satellite peak at 2 K in $h_\perp = 5.2$ Tesla.

fast normal modes, $0.653\ e^{-45t/T_1} + 0.215\ e^{-28t/T_1}$; the signal intensity, $M(t)$, begins to recover at a time scale comparable to the inversion pulse width. Accordingly, measurements of $1/T_1$ using the fourth satellite transition becomes more advantageous in the low temperature, low field regime, because its recovery curve is dominated by slower normal modes, $0.256\ e^{-15t/T_1} + 0.279\ e^{-10t/T_1}$. We present an additional example of the $1/T_1$ measurement using the fourth satellite at 2 K and $h_\perp = 5.2$ Tesla in Fig. S2.

## 2. Theoretical derivations of $1/T_1$ in the quantum Ising chain

Here we will summarize the derivations of the theoretical expressions of $1/T_1$ in the TFIC. Our notation will be the same as in [S3]. Some results will be specific to the nearest-neighbor Ising model, but most are more generally applicable to the vicinity of the quantum critical point of a generic one-dimensional Ising chain. In general, the NMR relaxation rate is defined by

$$\frac{1}{T_1} = \lim_{\omega\to 0} \frac{2T}{\omega} \int \frac{dk}{2\pi}\ |a_{hf}|^2\ \mathrm{Im}\chi(k,\omega) \tag{2a}$$

$$= \int \frac{dk}{2\pi}\ |a_{hf}|^2\ \mathrm{S}(k,\omega=0) \tag{2b}$$

$$= \int_{-\infty}^{+\infty} dt\ |a_{hf}|^2\ \mathrm{C}(x=0,t), \tag{2c}$$

where $a_{hf}$ represents the hyperfine coupling between the nuclear spin and the Pauli matrices $\sigma$, as defined by the hyperfine Hamiltonian $\hat{H}_{hf} = \hat{I}\cdot a_{hf}\cdot\hat{\sigma}$. We define the correlation function for Pauli matrices, and $\hbar = k_B = 1$ unless noted otherwise.

### 1. Renormalized Classical Regime

This region is characterized by an energy gap $\Delta \sim (g_c - g)$ and a $T = 0$ ordered moment $N_o \sim (g_c - g)^{1/8}$. The $N_o$ represents the ordered moment of an Ising chain at $T = 0$, and should not be confused with the 3D ordered moment induced by inter-chain couplings. By expressing our results in terms of $\Delta$ and $N_o$, they are generally valid *beyond* the nearest-neighbor model. For the specific case of the nearest-neighbor model, we have $\Delta = 2J(1-g)$ and $N_o = (1-g^2)^{1/8}$. The result for $C(x,t)$ may be found below (4.81) in Ref.[S3], and this leads to

$$\frac{1}{T_1} = |a_{hf}|^2 \frac{\pi N_o^2}{T} e^{+\Delta/T}. \tag{3}$$

Notice that $1/T_1$ is expected to diverge exponentially, even though there is an energy gap $\Delta$ in the excitation spectrum of the domain-wall quasi-particles. This is because NMR is a low energy probe, and $1/T_1$ in the RC regime is dominated by the low frequency spin fluctuations associated with the quasi-elastic mode of the 1D Ising chain induced by ferromagnetic short range order.

### 2. Quatum Critical Regime

Here, we have in imaginary time, $\tau$, from (4.106) in Ref. [S3] that

$$C(x=0,\tau) = ZT^{1/4} \frac{G_I(0)}{[2\sin(\pi T\tau)]^{1/4}}, \tag{4}$$

where $G_I(0) = 0.858714569$, and

$$Z = \lim_{\Delta\to 0} \frac{N_o^2}{\Delta^{1/4}}; \tag{5}$$

the value of $Z$ is a general result upon approaching from the ordered side, valid beyond the nearest-neighbor model.

From (4), we have the local susceptibility in imaginary time

$$\chi(x=0,\omega_n) = \int_0^{1/T} d\tau\ e^{i\omega_n\tau} C(x=0,\tau). \tag{6}$$

We evaluate the Fourier transform using (3.12), (3.22), and (3.24) of Ref.[S4], and obtain

$$\mathrm{Im}\ \chi(x=0,\omega_n) = \frac{ZG_I(0)}{T^{3/4}2^{1/4}\sqrt{\pi}\Gamma(1/8)\Gamma(5/8)} \times \sinh(\frac{\omega}{2T})|\Gamma(\frac{1}{8} - \frac{i\omega}{2\pi T})|^2. \tag{7}$$

This gives us

$$\frac{1}{T_1} = |a_{hf}|^2 \frac{Z}{T^{3/4}} \frac{G_I(0)\Gamma(1/8)}{2^{1/4}\sqrt{\pi}\Gamma(5/8)} = 2.13\ |a_{hf}|^2\ \frac{Z}{T^{3/4}}. \tag{8}$$

### 3. Quatum Disordered Regime

Here we can expect that $1/T_1$ diminishes exponentially in the quantum disordered regime due to the excitation gap, $|\Delta|$, and so

$$\frac{1}{T_1} \propto e^{-|\Delta|/T}, \tag{9}$$

where now $\Delta < 0$. However there is no explicit computation in the TIFC establishing this, and the pre-factor is unknown. There is no low frequency quasi-elastic mode, unlike the case of the RC regime.

## 3. Analysis of the $1/T_1$ data

We begin the analysis of $1/T_1$ in the QC regime. First, we combine eq. (5) with the results for the nearest-neighbor model, $\Delta = 2J(1-g)$ and $N_o = (1-g^2)^{1/8}$, and obtain $Z = J^{-1/4}$. We also introduce the hyperfine coupling $A_{hf}$ between the nuclear spin $I$ and electron spin $S$ through the hyperfine Hamiltonian $\hat{H}_{hf} = \hat{I}\cdot A_{hf}\cdot\hat{S}$.

That is, $a_{hf} = SA_{hf}$, and the $Co^{2+}$ is in a high-spin state with $S = 3/2$ due to the effects of the crystal field. Recalling that $1/T_1$ measured with an external magnetic field applied along the crystal b-axis probes the fluctuating hyperfine fields along the a- and c-axes, we may rewrite eq.(8) as

$$\frac{1}{T_1} = 2.13\ S^2\ \frac{|A_{hf}^{(a)}/\hbar|^2 + |A_{hf}^{(c)}/\hbar|^2}{2}\ \frac{\hbar}{(k_B J)^{1/4}(k_B T)^{3/4}}, \tag{10}$$

where we show $\hbar$ and $k_B$ explicitly. From the best fit of the $1/T_1$ data observed at 5.2 Tesla to eq.(10), we estimated the hyperfine form factor as $|a_{hf}/\hbar|^2 = |SA_{hf}/\hbar|^2 = S^2\ \frac{|A_{hf}^{(a)}/\hbar|^2+|A_{hf}^{(c)}/\hbar|^2}{2} = 7.6 \times 10^{14}$ ($s^{-2}$), using $J = 17.5$ K. As shown below, $A_{hf}$ is proportional to $\bar{g}\mu_B$, where $\bar{g}$ is the g-factor and $\mu_B$ represents the Bohr magneton. Therefore $|a_{hf}|^2$, and hence $1/T_1$, is proportional to $(\bar{g}\mu_B S)^2$. Physically, this is related to the fact that the fluctuating hyperfine field is generated by $Co^{2+}$ magnetic moments.

We can check the consistency of the fit based on the measurements of the NMR frequency shifts, $K^{(\alpha)} = \frac{A_{hf}^{(\alpha)}(0)}{\bar{g}\mu_B}\chi^{(\alpha)} + K_{chem}^{(\alpha)}$ ($\alpha = a$, b, or c-axis); $A_{hf}^{(\alpha)}(0)$ is the uniform $\mathbf{k} = \mathbf{0}$ component of the hyperfine coupling, and $K_{chem}^{(\alpha)}$ is a small temperature independent chemical shift. Thus $A_{hf}^{(\alpha)}(0)$ is related to $\frac{dK^{(\alpha)}}{d\chi^{(\alpha)}}$ as follows [S5];

$$\frac{A_{hf}^{(\alpha)}(0)}{\hbar} = \gamma_n N_A \bar{g}\mu_B\ \frac{dK^{(\alpha)}}{d\chi^{(\alpha)}}, \tag{11}$$

where the $^{93}$Nb nuclear gyromagnetic ratio is $\gamma_n/2\pi = 10.407$ MHz/Tesla, and $N_A$ is Avogadro's number. In Fig. S3, we plot $K^{(\alpha)}$ as a function of the molar magnetic susceptibility $\chi^{(\alpha)}$ measured along the corresponding orientations (see Fig. 2(c)), choosing $T$ as the implicit parameter. From the linear fit, we estimate the slope as $\frac{dK^{(\alpha)}}{d\chi^{(\alpha)}} = 0.386$, 0.221, and 0.311 for $\alpha = a$, b, and c, respectively.

To proceed, we need to relate $A_{hf}^{(\alpha)}/\hbar$ in eq.(10) with the uniform component $A_{hf}^{(\alpha)}(0)/\hbar$ in eq.(11). We point out that the Nb-O-Nb chain is inside an isosceles triangle formed by three Co-O-Co chains within the ab-plane, as shown in Fig. S4(a) and (b). For simplicity, we assume that the hyperfine interaction at the $^{93}$Nb site is dominated by the transferred hyperfine fields from two nearby Co-O-Co chains, and their strength, $\sim A_{hf}^{(\alpha)}(0)/2\hbar$, is comparable. In addition, since we conducted $1/T_1$ measurements above 2 K, we assume that the effects of the inter-chain interactions between adjacent Co-O-Co chains are negligibly small. Then the fluctuations of the transferred hyperfine fields from two chains may be considered independent, and hence additive. That is,

$$|A_{hf}^{(\alpha)}/\hbar|^2 \sim 2|A_{hf}^{(\alpha)}(0)/2\hbar|^2. \tag{12}$$

Combining eqs.(10), (11) and (12), we can estimate the only unknown parameter in our QC scaling analysis, the magnitude of the $Co^{2+}$ moment, as $\bar{g}\mu_B S \sim 3\mu_B$. This is in good agreement with the earlier report, $3.05\mu_B$ [S6]. Our estimation of $\bar{g}\mu_B S$ relies on simplistic assumptions, and hence should be considered provisional. Nonetheless, the overall consistency in our analysis of $1/T_1$ and $K$ indicates that the QC scaling theory outlined in the previous section II is valid at a quantitative level.

In the QD regime, the pre-factor of the leading $e^{-\Delta/T}$ term in eq.(9) is not known at this time, hence we fit the

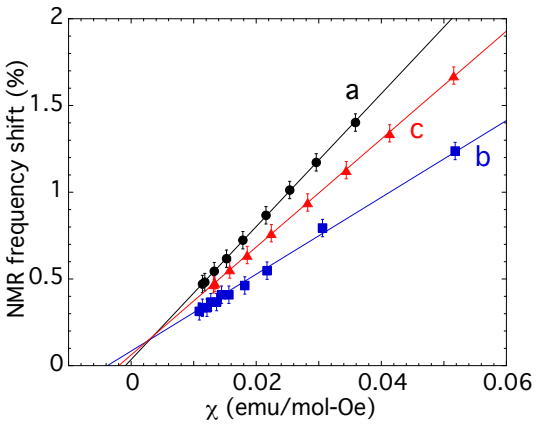


FIG. S3: The NMR frequency shift $K^{(\alpha)}$ vs. the bulk magnetic susceptibility $\chi^{(\alpha)}$, with $T$ as the implicit parameter ($\alpha = a$, b, or c). The straight lines are the best linear fits.

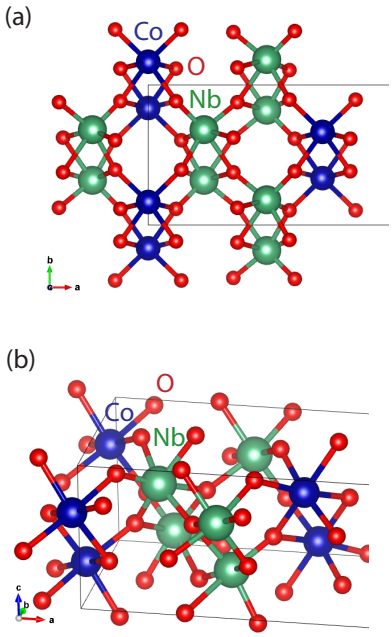


FIG. S4: Local geometry around the Nb sites. (a) A c-axis view of the crystal structure of $CoNb_2O_6$, and (b) the local geometrical configuration of Co and Nb. Notice that each Nb site is bonded with two adjacent Co-O-Co chains across O sites.

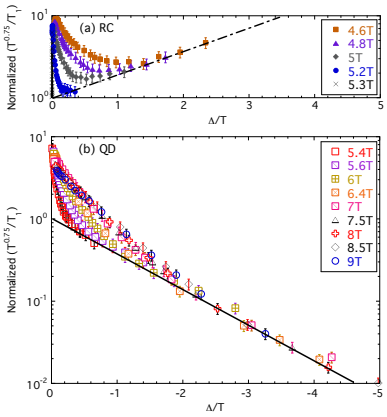


FIG. S5: The scaling plots of $T^{+0.75}/T_1$ as a function of $\Delta/T$ in (a) the RC regime, and (b) the QD regime. For clarity, we normalized the overall magnitude of $T^{+0.75}/T_1$ as unity for the QC regime. The dashed-dotted line in (a) is a guide-for-eyes, while the solid line in (b) represents $1/T_1 \propto e^{-|\Delta|/T}$.

$1/T_1$ data to the simple activation form in Fig. 4(a). In the case of the RC regime, we obtained the pre-factor of the leading $e^{+|\Delta|/T}$ term as $\sim 1/T$ in eq. (3). We found, however, that the observed divergent behavior of $1/T_1$ is weaker, perhaps because our experimental range of $T$ and $h_\perp$ is not deep inside the RC regime, or possibly due to the influence of additional terms in the Hamiltonian neglected in the theoretical calculations. Accordingly, we fit the $1/T_1$ data in the RC regime also with the simple exponential form, $1/T_1 \propto e^{+\Delta/T}$, as shown in Fig. 4(a).

For the $1/T_1$ data measured in $h_\perp \sim 5.3$ Tesla, our experimental temperature range and the resultant $\Delta$ estimated from Fig. 4(a) barely satisfy $T < |\Delta|$. To improve the accuracy of $\Delta$, we constructed the scaling plots of $T^{+0.75}/T_1$ as a function of $\Delta/T$ in Fig. S5. We first estimated the magnitude of $\Delta$ from Fig. 4(a), then made slight adjustments to improve the scaling collapse of the data. The final results of $\Delta$ are presented in Fig. 4(b) using ▲. We note that this procedure changes the value of $\Delta$ only by a few K.

## References

[S1] Momma, K. and Izumi, F. VESTA 3 for three-dimensional visualization of crystal, volumetric and morphology data, J. Appl. Crystallogr. **44**, 1272-1276 (2011).

[S2] Narath, A. Nuclear spin-lattice relaxation in hexagonal transition metals: Titanium. Phys. Rev. **162**, 320-332 (1967).

[S3] Sachdev, S. Quantum phase transitions, 1st Ed. (Cambridge University Press, Cambridge, 1999).

[S4] Sachdev, S. Senthil, T. and Shankar, R. Finite-temperature properties of quantum antiferromagnets in a uniform magnetic field in one and two dimensions. Phys. Rev. B **50**, 258-272 (1994).

[S5] Jaccarino, V. *Studies of the hyperfine interaction in transition metals*, in Proceedings of the international school of physics, Enrico Fermi, vol. XXXVII, p. 335 (Academic Press, New York, 1967).

[S6] Scharf, W. Weitzel, H. Yaeger, I. Maartense, I. and Wanklyn, B. M. Magnetic structures of $CoNb_2O_6$. J. Magn. Magn. Mater. **13**, 121-124 (1979).